


Universal Design of Ultra-Broadband and Ultra-Compact High Order Mode Pass Filters Based on Enhanced Absorption in Ultrathin Metal Layers

Qian Li, Xin Hao, and Yanli Zhao 

Abstract—In hybrid plasmonic Si waveguides integrated with ultrathin Au stripes, mode hybridization effects between quasi-TE modes of different orders and various bound modes are first presented. Enabled by nearly complete mode-selective absorption attributed to the enlarged mode propagation attenuation (MPA) coefficient for lower-order quasi-TE modes under circumstances of mode hybridizations, multi-segment tapered structures are theoretically proposed to constitute high order mode (HOM) pass filters. It is believed that these innovative observations would have potential applications in the ultra-compact on-chip mode division multiplexing (MDM) systems, and provide inspirations for the development of multimode photonics.

Index Terms—Mode hybridization, mode division multiplexing, multimode photonics.

I. INTRODUCTION

WITH the rapidly growing demands for data rates of optical communication in recent years, mode division multiplexing (MDM) [1]–[6] system has been widely addressed as a promising technology, which can overcome the capacity bottleneck of traditional single-mode fiber (SMF) transmission system by providing another independent degree of freedom for multiplexing types except for wavelength and polarization. In a MDM system, the significant modal crosstalk caused by imperfect de-multiplexing may give rise to a deterioration of the signal-to-noise ratio (SNR). Besides, the arbitrary mode routing puts forward a strict requirement for mode selective transmission. Similar to the polarizer [7] for the polarization

manipulation issues, mode filter, which can obstruct the undesired modes while passing through the desired modes efficiently, has drawn attention from researchers in recent years [8]–[24].

By virtue of the stronger confinement for low order modes (LOMs) in the traditional waveguide, it is a more challenging and attractive topic to develop the high order mode (HOM) pass (LOM block) filter. By utilizing mode conversion with asymmetric directional coupler (ADC) [8], Mach-Zehnder interference (MZI) incorporated with Y-junction [9], [10], and phase-shifted long-period grating (LPG) [11], the undesired LOMs can be converted to HOMs and be stripped off by an adiabatic taper when mode cut-off condition is satisfied. To compensate for the nontrivial spectral fluctuation caused by the stochastic input phase relationship [9], a phase-insensitive mode filter [12] was proposed, with a Y-junction and multimode interference (MMI), the input TE_0 and TE_1 mode are split into in-phase and anti-phase TE_0 pairs and form image of TE_0 and TE_1 mode at the side and center output ports, respectively. Moreover, effective mode filtering enabled by phase matching in the 1D photonic crystal [13] and grating-based contra-directional coupler [14] have also been verified by experiments. By the structure in which a SMF is inserted between two few-mode fibers [15], a destructive interference happens between beams of LP_{01} mode in core and cladding section during the propagation in SMF, spatial mode-selective transmittance in all-fiber structure also has been achieved. In addition, it has been demonstrated experimentally or theoretically that graphene [16]–[19] and VO_2 [20] integrated mode filters can realize selective absorption through special placement adopted for mode field distribution nature. There are other works utilizing the inverse design method [21], [22] to achieve mode-selective pass between TE_0 and TE_1 mode, which can achieve operation bandwidth of more than 100 nm within the length of a few microns while maintaining low excess loss (EL). In addition, with the utilization of hyperbolic metamaterials [23] and plasmonic bridged subwavelength gratings (BSWGs) [24], TM-dependent HOM pass filters are also developed in theory as a result of large radiation loss and metal absorption loss for LOMs.

To conclude, most of the previously reported works merely focus on the manipulation of fewer modes, usually two or

Manuscript received November 11, 2021; revised December 14, 2021; accepted December 25, 2021. Date of publication December 31, 2021; date of current version February 2, 2022. This work was supported in part by the National Key R&D Program of China under Grant 2018YFB2200204, in part by the Science and Technology Project from Wuhan City under Grant 2020010601012162, and in part by the Open-Foundation of Key Laboratory of Laser Device Technology, China North Industries Group Corporation Limited under Grant KLLDT202002. (Corresponding author: Yanli Zhao.)

Qian Li and Yanli Zhao are with the Wuhan National Laboratory for Optoelectronics, Huazhong University of Science and Technology, Wuhan 430074, China (e-mail: liqian930218@hust.edu.cn; yanlizhao@mail.hust.edu.cn).

Xin Hao is with the Key Laboratory of Laser Device Technology, China North Industries Group Corporation Limited, Chengdu 610041, China (e-mail: emil-007@163.com).

Digital Object Identifier 10.1109/JPHOT.2021.3139301

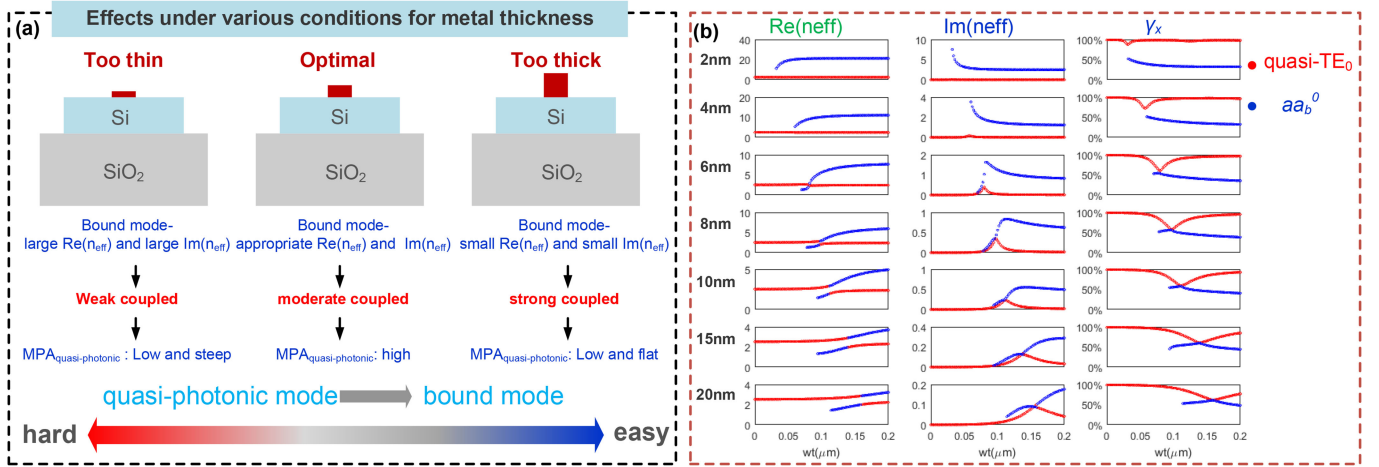


Fig. 1. (a) Characteristics of hybridization effects between quasi-photonic mode and bound mode under various gold thicknesses. (b) Effective indices and TE polarization fraction (defined as $\gamma_x = \frac{\iint |E_x^2| dx dy}{\iint |E_x^2| dx dy + \iint |E_y^2| dx dy}$) [28]) for quasi-TE₀ mode and aa_b⁰ mode with different gold thickness.

three. Though the universal scheme based on mode conversion facilitated by ADC [8] can achieve operation for modes with arbitrary order, a large device length is still required for the purpose of adiabatic coupling between the fundamental mode and HOM. The absorption-based ones are usually suffering from low compactness [17], [18], large EL [20] and unsatisfactory modal extinction ratio (ER) [18], owing to weak absorption coefficient and small MPA difference between modes remaining to be distinguished. Moreover, some grating-type mode filters [14] have limited bandwidth since a phase-matching condition can only be satisfied within a narrow wavelength span. Whereas the wide operation band can be realized at the expense of either EL for favorable modes or device length. Up to now, an ultra-compact, low-loss, broadband mode filter with high design scalability is rarely reported.

In this work, a versatile design approach for a novel HOM pass filter is proposed in theory, based on the enhanced absorption in ultrathin metal stripes induced by mode hybridization effects between quasi-photonic modes and bound modes. By centering metal stripes at the zero planes of field distribution for the desired HOM, little interaction between HOM and metal occurs, thus an ultralow propagation loss caused by metal absorption can be realized for HOM incidence. While all LOMs are supposed to attenuate rapidly owing to the nearly complete absorption in metal stripes resulting from significant mode hybridization effects with various bound modes. The intuitive approach can be applicative for arbitrary HOM pass filter. We anticipate the newly presented series of mode hybridization effects to suggest the design of ultra-compact mode control devices for multimode photonics and MDM systems.

II. DESIGN PRINCIPLE

In this work, three types of plasmonic waveguide, consisting of multimode silicon on insulator (SOI) waveguide with a 220 nm-thick top layer and ultrathin Au stripes, are investigated as design prototypes. Mode fields and effective indices are

calculated by finite difference eigenmode (FDE) solver in Mode solutions software [25]. The light propagation processes are simulated by FDTD Solutions software [25]. All the optical constants used in our simulations are from [26]. The wavelength in our design is mostly fixed at 1.55 μm without special explanation. The naming rules for bound modes and simulation settings are included in Appendix.

A. Choice of Metal Thickness

For the design of mode filter based on plasmonic waveguide, the choice of gold thickness is critical and worthy to be investigated. As displayed in Fig. 1(a)(b), mode hybridization effects between quasi-TE₀ mode and aa_b⁰ mode occur at different metal widths under various gold thicknesses. One can be concluded is that when the gold film is too thin, the MPA rise of the quasi-TE mode is very limited, owing to weak hybridization resulted from large refractive indices differences between two modes. When the metal thickness increases to 6–8 nm, the coupling effect between these two hybrid modes is enhanced slightly and the MPA value for quasi-TE mode can reach 12.32–14.08 dB/μm (The corresponding imaginary part of mode refractive index is 0.35–0.4). With a thicker gold film (typically larger than 15 nm) implanted on the top of Si layer, the mode field of the aa_b⁰ mode extends into Si gradually, thus both the real and imaginary parts of effective refractive indices for aa_b⁰ mode decrease significantly, and the MPA enhancement for hybrid modes is substantially weakened. From our mode analyses, gold stripe with a thickness of 8 nm is considered as an optimum choice to trigger MPA enhancement for hybrid modes to a great extent.

B. Single Metal Stripe

For plasmonic waveguide integrated with one metal stripe, the mode naming rules is originated from [27]. As it can be seen from Fig. 2(a), when w_{Si} is 1.2 μm, mode hybridization effects occur successively between aa_b⁰ and quasi-TE₂, aa_b⁰

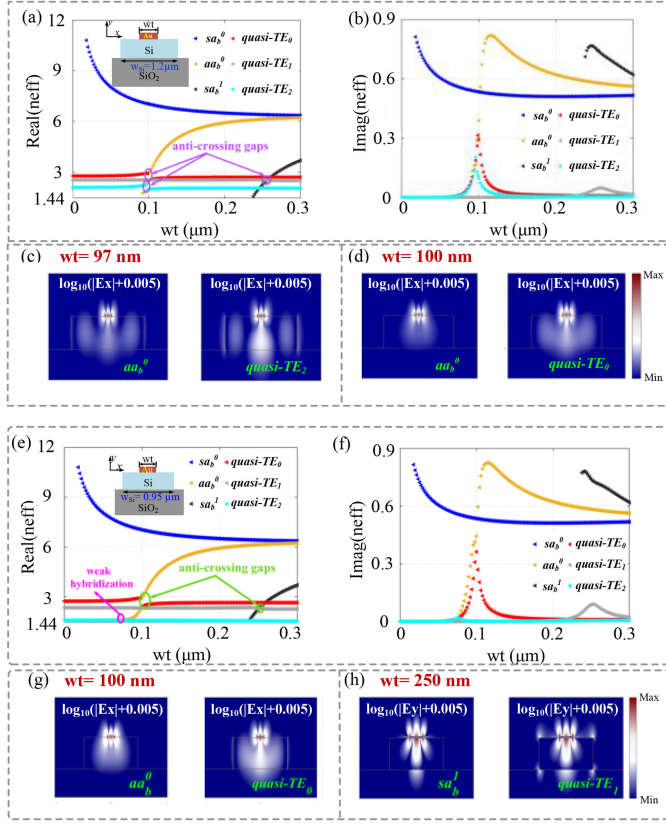


Fig. 2. (a) Real parts and (b) Imaginary parts of mode effective indices varying with wt when $w_{Si} = 1.2 \mu\text{m}$; electric field profiles of hybridized modes when (c) $wt = 97 \text{ nm}$; (d) $wt = 100 \text{ nm}$. (e) Real parts and (f) Imaginary parts of mode effective indices varying with wt when $w_{Si} = 0.95 \mu\text{m}$; electric field profiles of hybridized modes when (g) $wt = 100 \text{ nm}$; (h) $wt = 250 \text{ nm}$.

and quasi-TE₀ modes (see in Fig. 2(c)(d)), and also between quasi-TE₁ mode and sa_b^1 modes, which can be confirmed by the anti-crossing phenomena [28], [29] with “gap” between the two corresponding curves of effective indices for hybridized modes. Different from the hybridization effects between TM and high-order TE modes in lossless Si waveguides [28], [29], quasi-TE_{*n*} modes would obtain large MPAs under circumstance of hybridization with bound modes, which can be revealed by the rise in imaginary part curves for quasi-TE₀ and quasi-TE₂ modes in Fig. 2(b).

Combined with previous investigations [30], [31], it can be extended to general cases that quasi-TE_{2*n*} and quasi-TM_{2*n*+1} modes would be hybridized with aa_b^m modes, while quasi-TE_{2*n*+1} and quasi-TM_{2*n*} modes would be hybridized with sa_b^k modes (m and n are both natural numbers, k is a positive integer) with certain metal widths, provided that the Si waveguide is wide enough.

Nevertheless, the degree of hybridization for quasi-TE₂ mode is various with different w_{Si} , when quasi-TE₂ mode is weakly confined in a Si waveguide as narrow as $0.95 \mu\text{m}$, the large mode field mismatch between quasi-TE₂ mode and aa_b^0 mode make them hardly hybridized with each other. As shown in Fig. 2(e), (f), the Real(neff) curves of aa_b^0 and quasi-TE₂ modes intersect

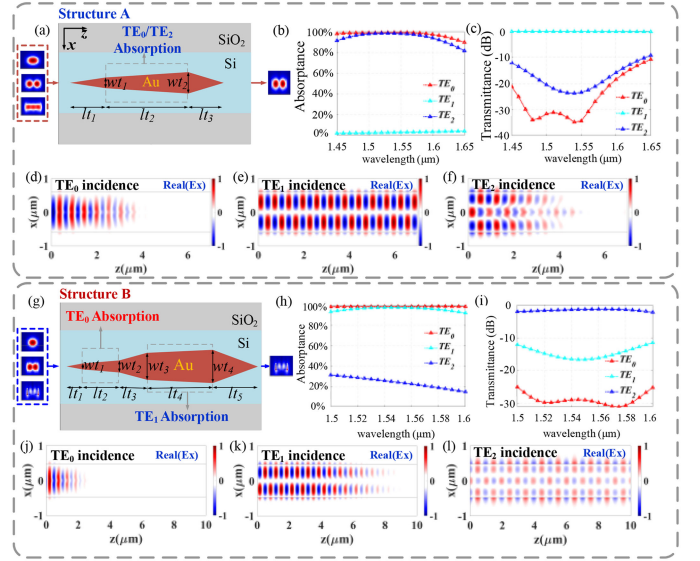


Fig. 3. (a) Schematic diagram, (b) Absorption rate, (c) Transmittance of Structure A; Real part of E_x components profiles at $\lambda = 1.55 \mu\text{m}$ with input: (d) TE₀ mode (e) TE₁ mode (f) TE₂ mode for structure A. (g) Schematic diagram, (h) Absorption rate, (i) Transmittance of Structure B; Real part of E_x components profiles with input: (j) TE₀ mode (k) TE₁ mode (l) TE₂ mode for structure B. Geometric parameters for structure A: $w_{Si} = 1.2 \mu\text{m}$, $lt_1 = 0.2 \mu\text{m}$, $lt_2 = 5 \mu\text{m}$, $lt_3 = 0.3 \mu\text{m}$. Structure B: $w_{Si} = 0.95 \mu\text{m}$, $lt_1 = 0.2 \mu\text{m}$, $lt_2 = 3 \mu\text{m}$, $lt_3 = 0.3 \mu\text{m}$, $lt_4 = 6 \mu\text{m}$, $lt_5 = 0.2 \mu\text{m}$.

almost directly, and the Imag(neff) of quasi-TE₂ mode does not present an evident rise, comparing with the case for $w_{Si} = 1.2 \mu\text{m}$. Hence the absorption of quasi-TE₂ mode can be flexibly controlled by simply adjusting w_{Si} . In addition, there are still strong mode hybridization effects between quasi-TE₀ and aa_b^0 modes (and also between quasi-TE₁ and sa_b^1 mode), which can be confirmed by the anti-crossing gaps circled out by green lines in Fig. 2(e) and the significant MPA increments for quasi-TE₀ and quasi-TE₁ mode, when wt is near $0.1 \mu\text{m}$ and $0.25 \mu\text{m}$, respectively (as shown in Fig. 2(f)). Also, similar electric field distributions of the two pairs of hybridized modes are shown in Fig. 2(g)(h).

According to the mode analyses above, two types of mode filters are proposed and depicted in Fig. 3(a) and (g). The operation principles of the two structures are briefly summarized as follows: in structure A, the mode hybridization effects between quasi-TE₀/TE₂ and aa_b^0 mode are triggered simultaneously in the second taper with a width range of $wt_1 - wt_2$ ($0.085 - 0.105 \mu\text{m}$), and the hybridized modes get absorbed efficiently. While TE₁ mode is barely unaffected during the propagation process. In structure B, quasi-TE₀ and quasi-TE₁ mode are separately absorbed in the second and fourth tapered parts with a metal width range of $wt_1 - wt_2$ ($0.09 - 0.11 \mu\text{m}$) and $wt_3 - wt_4$ ($0.24 - 0.26 \mu\text{m}$), attributing to the enhanced MPAs caused by the mode hybridization effects between quasi-TE₀ and aa_b^0 , quasi-TE₁ and sa_b^1 modes. Whereas quasi-TE₂ mode with low MPA can be transmitted efficiently. In structure A and B, the first and last taper facilitate efficient coupling between pure TE mode and quasi-TE mode.

To characterize the propagation process in structure A and B, 3D-FDTD method is utilized. As illustrated in Fig. 3(b), the absorption rates for TE₀ and TE₂ incidences in structure A are above 90% for wavelength from 1.45 μm to 1.62 μm. The EL of TE₁ mode is only 0.16 dB, which is an impressive value, as shown in Fig. 3(c). Meanwhile, an ER of 20 dB with bandwidths of 140 nm (1450–1590 nm) and 70 nm (1500–1570 nm) for TE₁ mode against TE₀ and TE₂ mode is theoretically achieved, respectively. The propagation electric field profiles in xz plane for λ = 1.55 μm are shown in Fig. 3(d)-(f), which indicate efficient transmitting for TE₁ incidence and prohibition for TE₀/TE₂ input. As for structure B, one can be seen from Fig. 3(i) that the rejection of TE₁ mode is not particularly ideal, since the mode hybridization between quasi-TE₁ and *sa_b*⁰ mode is weaker (than that between quasi-TE₀ and *aa_b*⁰ mode), an ER of 15 dB is theoretically realized with a bandwidth of only 15 nm (1540–1555 nm). The propagation field profiles in Fig. 3(j)(k) show effective stripping of quasi-TE₀ and quasi-TE₁ mode which are respectively realized after the second and fourth taper for the wavelength of 1.55 μm. However, the EL of TE₂ mode is still up to 1.5 dB, as a consequence of the absorption by metal stripe within long propagation length. Notably, structure B can operate only if the TE₂ mode is weakly confined (as shown in Fig. 3(l)), which, however, inevitably imposes bandwidth limitations.

C. Dual and Triple Metal Stripes

Enlightened by the above observations, further attempts are made by implanting two and three Au stripes on the multimode Si waveguide with widths of 1.1 μm and 1.6 μm. The ultrathin Au stripes are symmetric in the horizontal direction with an interval of *dx*. By adjusting the value of *dx*, the MPA and TE polarization fraction (defined as $\gamma_x = \frac{\iint |E_x|^2 dx dy}{\iint |E_x|^2 dx dy + \iint |E_y|^2 dx dy}$ [28]) of each quasi-TE_{*n*} mode when *wt* = 0.1 μm are plotted in Fig. 4(a) and (d).

For each quasi-TE_{*n*} mode, the variation trend of MPA is in direct contradiction to that of TE polarization fraction. It can be predicted that the increase in MPA for quasi-TE_{*n*} mode is originated from a stronger interaction with the bound mode with large MPA. Particularly, an ultralow MPA for quasi-TE₂ and quasi-TE₃ mode is achieved as *dx* is about 0.4 μm (as shown in Fig. 4(a) and (d)), which can be attributed to the minimized perturbation of bound mode as each metal stripe is centered at the dips of the *E_x* horizontal profile curve for TE₂/TE₃ mode (as shown in Fig. 4(b) and (e)), resembling the statement in [18]. Also, the dominated *E_x* field and the weak intensity near the metal edge in Fig. 4(c) and (f) prove the high TE polarization purity (93%/95%) for quasi-TE₂/quasi-TE₃ mode when *dx* = 0.4 μm. As for the condition with other *dx* values, strong field intensities exhibit at the interface of metal and Si for quasi-TE₂/quasi-TE₃ mode, which is similar to a plasmonic mode, thus the MPAs for these cases are considerable.

To identify the underlying origins of the considerable MPAs for LOMs, the dependences of mode effective indices on metal width *wt* when *dx* is 0.4 μm are investigated by FDE solver. In

Fig. 4(g)(h), both the real and imaginary parts curves for various *-sa_b*⁰ modes are highly coincident. The anti-crossing characteristics of Real(*neff*) curves reveal the existence of hybridization effect between quasi-TE₀ and *a-aa_b*⁰ mode, and also between quasi-TE₁ and *s-aa_b*⁰ mode. The widths of the metals required for the two hybridization effects to occur are not uniform but very close to one another. In the hybridization areas, one can be seen from Fig. 4(h) is that the MPAs of quasi-TE₀ and quasi-TE₁ modes obtain a significant rise and exhibit an extremum at the metal widths corresponding to the “switching” points of Real(*neff*) curves. Here the modal fields under two cases (i.e., *wt* = 99 nm and 96 nm) are also presented in Fig. 4(i)(j), from which the comparable *E_x* and *E_y* components for the two pairs of modes indicate strong mode hybridization. After the mode hybridization areas, the effective indices of *a-aa_b*⁰ and *s-aa_b*⁰ modes tend to be consistent and the MPAs of quasi-TE₀ and quasi-TE₁ mode drop dramatically. Besides, the effective indices of quasi-TE₂ mode almost remain unchanged as *wt* is in the range of 0–0.2 μm, thus quasi-TE₂ mode would behave as a guided-mode confined mostly in Si with ultralow MPA as expected in Fig. 4(a). Similarly, for the case of plasmonic waveguide integrated with three ultrathin metal stripes, as shown in Fig. 4(k)(l), there exist mode hybridization effects between quasi-TE₀ and *i-aa_b*⁰, quasi-TE₁ and *e-aa_b*⁰, quasi-TE₂ and *o-aa_b*⁰ modes, respectively. The similar modal field profiles are shown in Fig. 4(m)-(o).

Benefiting from the ultralow MPA of HOM and large MPA of LOMs indicated from mode analyses in the two plasmonic waveguide configurations, TE₂ mode and TE₃ mode pass filter can be proposed. For the structure shown in Fig. 5(a) and (g), the first triangular taper can make incident modes convert to quasi-photonic modes without decoupling to pure Si waveguide. In the second taper, the undesired LOMs couple to hybrid modes with large MPAs and get absorbed simultaneously. While the desired HOM propagates with low MPA in the three sections mentioned above and is coupled to original HOM by the inverted taper efficiently.

Through numerical simulations performed by 3D-FDTD method, the absorption efficiency of the metal stripes for the incident TE₀ and TE₁ modes in the wavelength range from 1480 nm to 1620 nm can reach almost 100%, as Fig. 5(b) shows. Moreover, from the normalized transmittance spectra shown in Fig. 5(c), an ER of 20 dB is achieved theoretically in wavelength ranges of 1460–1650 nm (TE₂-TE₁) and 1425–1635 nm (TE₂-TE₀). In general, the ER is better than 20 dB over a ~175 nm (1460–1635 nm) wavelength span. The light propagation performances of the TE₂ mode pass filter at wavelength of 1.55 μm are demonstrated in Fig. 5(d)-(f). It can be seen that the TE₀ and TE₁ mode are gradually decayed until they almost disappear, as energy accumulates towards the metal/Si interface and is eventually absorbed by Au stripes. While the TE₂ mode passes through almost transparently, without resulting in any undesirable scattering/reflecting or inter-mode coupling.

For TE₃ mode pass filter shown in Fig. 5(g), the group velocity is nearly the same as that of in the pure SOI waveguide for TE₃ mode incidence, which can be revealed from Fig. 5(h). The

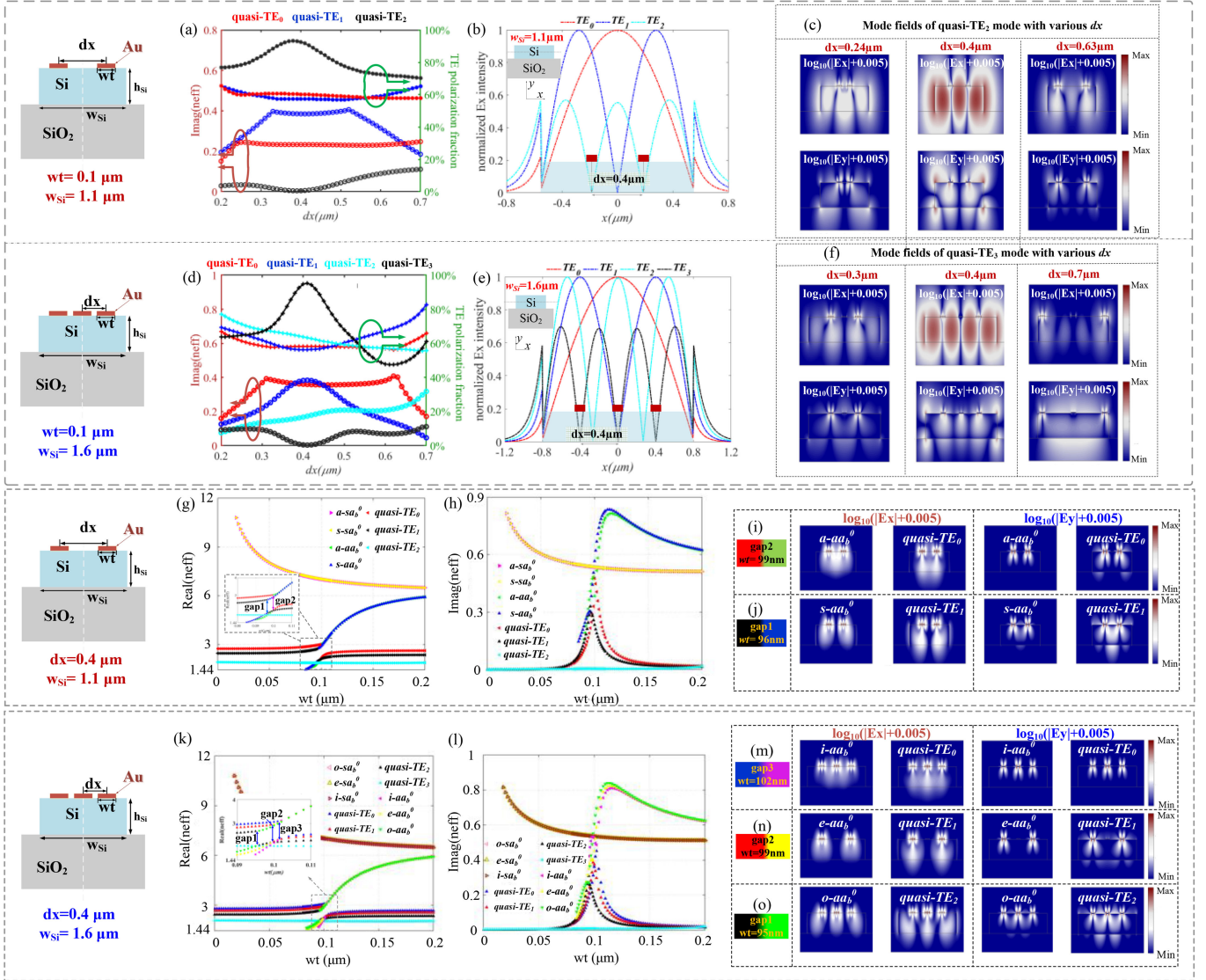


Fig. 4. (a) Imaginary parts of effective indices and TE polarization fraction for quasi-TE₀-quasi-TE₂ modes as dx increases. Structure parameters: $w_{Si} = 1.1 \mu\text{m}$, $wt = 0.1 \mu\text{m}$. (b) Electric field profiles of TE₀-TE₂ modes in $1.1 \mu\text{m}$ -wide Si waveguide. (c) Modal fields of quasi-TE₂ mode with various dx . (d) Imaginary parts of effective indices and TE polarization fraction for quasi-TE₀-quasi-TE₃ modes as dx increases. Structure parameters: $w_{Si} = 1.6 \mu\text{m}$, $wt = 0.1 \mu\text{m}$. (e) Electric field profiles of TE₀-TE₃ modes in $1.6 \mu\text{m}$ -wide Si waveguide. (f) Modal fields of quasi-TE₃ mode with various dx . (g) Real parts and (h) imaginary parts of mode effective indices with varying wt , electric field profiles of hybridized modes when (i) $wt = 99 \text{ nm}$; (j) $wt = 96 \text{ nm}$ for dual-metal stripe configuration. (k) Real parts and (l) imaginary parts of mode effective indices with varying wt , electric field profiles of hybridized modes when (m) $wt = 102 \text{ nm}$, (n) $wt = 99 \text{ nm}$, (o) $wt = 95 \text{ nm}$ for triple-metal stripe configuration.

absorption rate and normalized transmission response spectra for each launched mode are shown in Fig. 5(i)(j). For the case of $w_{Si} = 1.6 \mu\text{m}$, the absorptance of TE₀-TE₂ modes is approaching 100% in wavelength range of $1.35\text{--}1.62 \mu\text{m}$ and exceeds 90% in the wavelength range of $1.3\text{--}1.7 \mu\text{m}$. The EL_{TE3} degrades significantly as wavelength increases and approaches 2.2 dB for $1.7 \mu\text{m}$ wavelength. The bandwidth $BW_{ER>20\text{dB}}$ for achieving a 20 dB rejection ratio of TE₀-TE₂ modes over TE₃ mode can reach up to 300 nm ($1350\text{--}1650 \text{ nm}$). Fortunately, the characteristic of EL_{TE3} can be optimized by altering w_{Si} from $1.6 \mu\text{m}$ to $2.4 \mu\text{m}$, as dx is adjusted from $0.4 \mu\text{m}$ to $0.6 \mu\text{m}$ accordingly. When $w_{Si} = 2.4 \mu\text{m}$, there exists EL_{TE3} as low as

$0.14\text{--}0.61 \text{ dB}$ in wavelength range of $1.2\text{--}1.7 \mu\text{m}$, while with a slightly deteriorated but acceptable $BW_{ER>20\text{dB}}$ of 210 nm ($1410\text{--}1620 \text{ nm}$) compared to the case of $w_{Si} = 1.6 \mu\text{m}$. Moreover, Fig. 5(k)-(n) display the E_x profiles in the xz plane as TE₀-TE₃ modes are launched from the input port (when $w_{Si} = 1.6 \mu\text{m}$). As expected, the almost complete blocking for transmission of LOMs (TE₀-TE₂ mode) can be realized within different propagation lengths for various wavelengths, while there is no obvious intensity attenuation along the propagation direction under TE₃ incidence. Therefore, the proposed TE₃ mode pass filter presents wide spectrum filtering functionality for LOMs.

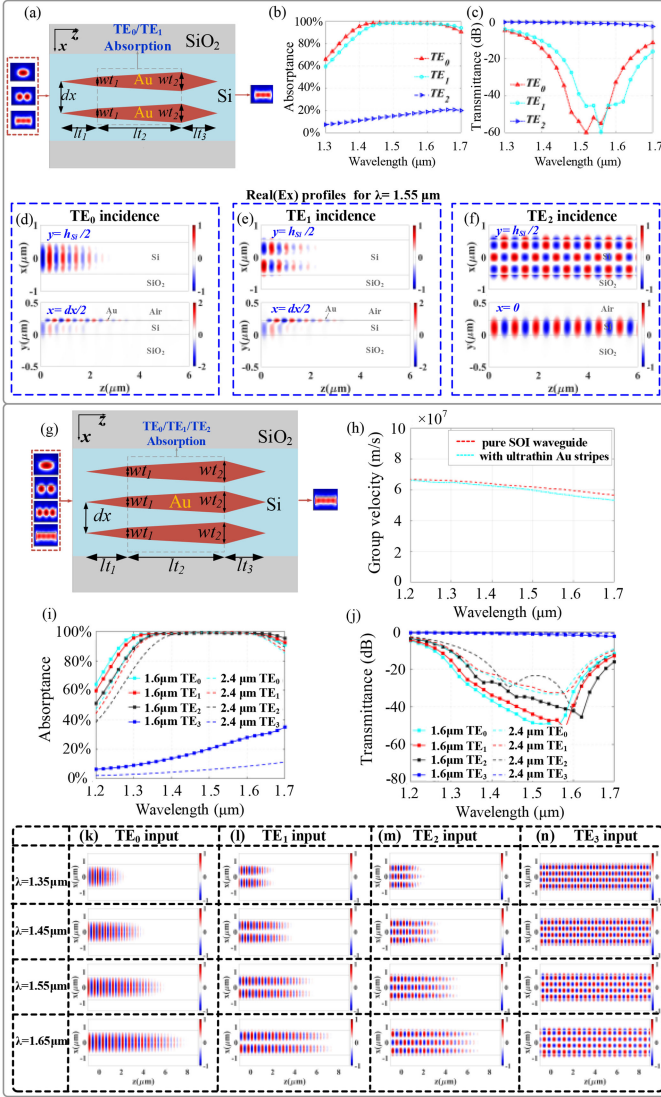


Fig. 5. (a) Schematic diagram of the proposed TE_2 mode pass filter. (b) Absorption rate and (c) transmittance for TE_0 - TE_2 incidence. Electric filed profiles ($Real(E_x)$) for TE_0 - TE_2 incidences: (d) TE_0 incidence; (e) TE_1 incidence; (f) TE_2 incidence; Structure parameters: $w_{Si} = 1.1 \mu\text{m}$, $w_{T1} = 0.09 \mu\text{m}$, $w_{T2} = 0.11 \mu\text{m}$, $dx = 0.4 \mu\text{m}$, $l_{T1} = 0.2 \mu\text{m}$, $l_{T2} = 5 \mu\text{m}$, $l_{T3} = 0.3 \mu\text{m}$. (g) Schematic diagram of the proposed TE_3 mode pass filter. (h) Comparison of group velocity between our proposed TE_3 mode pass filter and SOI waveguide ($1.6 \mu\text{m}$ wide) under TE_3 mode incidence. (i) Absorption rate and (j) transmittance for TE_0 - TE_3 incidence when $w_{Si} = 1.6 \mu\text{m}$ ($dx = 0.4 \mu\text{m}$) and $2.4 \mu\text{m}$ ($dx = 0.6 \mu\text{m}$), respectively. Electric filed profiles ($Real(E_x)$) for TE_0 - TE_3 incidences at various wavelengths: (k) TE_0 incidence; (l) TE_1 incidence; (m) TE_2 incidence; (n) TE_3 incidence; Structure parameters: $w_{T1} = 0.07 \mu\text{m}$, $w_{T2} = 0.11 \mu\text{m}$, $l_{T1} = 0.2 \mu\text{m}$, $l_{T2} = 8 \mu\text{m}$, $l_{T3} = 0.3 \mu\text{m}$.

III. CONCLUSION

Additionally, comparisons between our designs and previously reported works are made and presented in Table. I. The proposed HOM filter performs well on almost all metrics, including device footprint and bandwidth, as well as EL and ER. Notably, The TE_2 and TE_3 mode pass filters can achieve low EL and ultra-broadband bandwidth with ultra-compact footprints in theory, which are the most compact HOM pass filters with the broadest operating wavelength range up to now.

In this work, the mode hybridization effects between quasi- TE_{2m} (or quasi- TM_{2m+1}) and aa_b^n mode, as well as quasi- TE_{2m+1} (or quasi- TM_{2m}) and sa_b^k (k is a positive integer, m

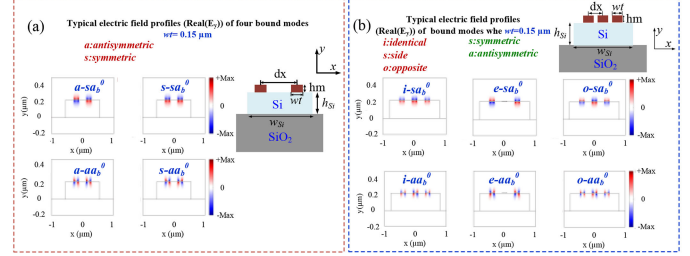


Fig. 6. Typical bound mode field profiles in (a) dual-metal stripe configuration; (b) triple-metal stripe configuration. $\lambda = 1.55 \mu\text{m}$.

and n are both natural numbers) modes in a hybrid plasmonic waveguide integrated with a metal stripe are first presented. Moreover, by implanting more metal stripes on multimode Si waveguide, hybridization effects between quasi- TE mode of different order and various aa_b^0 modes are also theoretically observed. The existence of mode hybridization makes it possible to achieve nearly complete absorption for various orders of TE modes within a short length ($< 10 \mu\text{m}$) in our proposed HOM pass filter architectures. Through the above simulations, a universal method for constructing a TE_n (n is a positive integer) mode pass filter can be obtained, i.e., by placing n metal stripes with favorable width at the center of dips for TE_n mode electric field curve, the MPA of quasi- TE_n mode can be minimized. Simultaneously, there would exist n pairs of hybridized modes, i.e., various aa_b^0 and quasi- TE_k ($k = 0, 1, 2, \dots, n-1$) mode, between which hybridization effects are supposed to happen, thereby a high-efficiency pass filter for TE_n mode can be obtained by nearly complete absorption of all undesired TE_k ($k = 0, 1, 2, \dots, n-1$) modes. It needs to be emphasized that the hybridization appears not only for our proposed configurations. There exist candidates for this design strategy, such as Ag and Al, whose refractive index is composed of a small real part and a large imaginary part. Additionally, by employing appropriate waveguide geometry, TM mode-dependent hybridization can also be triggered to accomplish the function of TM HOM pass filters. To conclude, this design strategy has extremely high flexibility and expansibility.

However, extremely advanced technical means are still required to put this design into actual fabrication, since it remains a challenge to form a smooth, uniform, ultrathin metal film on Si substrate [32], [33]. Discussions about the influence caused by thickness and width fabrication errors are included in Appendix C. Nevertheless, we argue that the architecture would be suitable for high-density Si photonic integrated circuits (PICs) in the near future, attributing to the negligible scattering/reflection loss and ultra-compact size. And we also hope the mode analyses in this work may open up new opportunities for multimode photonics to further shrink the size of functional devices (such as mode converter, polarization splitters, mode splitters, etc.) by tens or even hundreds of times.

APPENDIX

A. Naming Rules of Bound Modes

To clarify the bound modes involved in the plasmonic waveguides, the typical mode field profiles are displayed in Fig. 6(a)(b). Following the nomenclature for bound modes in [27], the two

TABLE I
COMPARISONS OF REPORTED HIGH ORDER MODE PASS FILTERS WITH OUR PROPOSED STRUCTURES

Structures	Size (μm)	BW (nm)	EL (dB)	ER (dB)	Device function
ADC ^(a) (Exp.)[8]	10000	40	0.47	20	TE ₀ /TE ₁ /TE ₂ /TE ₃ input, TE ₃ pass
MZI+Y-junction (Exp.)[9]	11000	35	0.52	37	TE ₀ /TE ₁ input, TE ₁ pass
Phase-shifted LPG ^(b) (Exp.)[11]	26000	>140	>1.5	~18	E ₁₁ /E ₁₂ /E ₂₁ input, E ₁₂ /E ₂₁ pass
MMI+Y-junction (Exp.)[12]	150	>35	<1.5	>15	TE ₀ /TE ₁ input, TE ₁ pass
1D PC ^(c) grating (Exp.)[13]	15	>100	1.8	50	TE ₀ /TE ₁ input, TE ₁ pass
SWG-based CDC ^(d) (Exp.)[14]	12	35	<1.4	>21	TE ₀ /TE ₁ input, TE ₁ pass
Graphene absorption (Exp.)[16]	11000	165	2	17	E ₁₁ /E ₁₂ /E ₂₁ input, E ₁₂ /E ₂₁ pass
Inverse design (Exp.)[22]	3	60	<1	>15	TE ₀ /TE ₁ input, TE ₁ pass
Plasmonic BSWG ^(e) (Sim.)[24]	260	150	0.63	15	TM ₀ /TM ₁ input, TM ₁ pass
Graphene absorption (Sim.)[18]	200	-	8.4	5.37	TE ₀ / TE ₁ /TE ₂ input, TE ₂ pass
This work (Sim.)	5.5	140	0.16	>20	TE ₀ /TE ₁ input, TE ₁ pass
	5.5	175	0.9	>20	TE ₀ / TE ₁ /TE ₂ input, TE ₂ pass
	8.5	300	0.9	>20	TE ₀ /TE ₁ /TE ₂ /TE ₃ input, TE ₃ pass
		210	0.3	>20	TE ₀ /TE ₁ /TE ₂ /TE ₃ input, TE ₃ pass

^(a)ADC, asymmetric directional coupler; ^(b)LPG, long period grating; ^(c)PC, photonic crystal; ^(d)CDC, contra-directional coupler; ^(e)BSWG, bridge subwavelength grating.

letters after the dashes describe the symmetry of E_y field distribution in the horizontal and vertical direction, respectively. The subscript ‘b’ means ‘bound’, and the superscript ‘m’ stands for the order number of bound mode. For the case of dual-metal stripe, the preferred letters ‘s’ and ‘a’ stand for “symmetric” or “antisymmetric” respectively (which describe the symmetry of E_y components with y -axis). For triple metal stripe configuration, the field profiles of typical bound modes are shown in Fig. 6(b), among which the preferred ‘i’ and ‘o’ respectively represent the polarity of E_y components around center stripe are ‘identical’ and ‘opposite’ with that of the stripes at two sides, and the letter ‘e’ denotes that there are only strong filed profiles around two metal stripes at the two ‘edges’.

B. Details About FDTD Simulation Settings

The perspective view of our settings is shown in Fig. 7(a). The boundary conditions for each direction are set to the perfect match layer (PML). The global mesh is set as “auto non-uniform (mesh order 8)”. Owing to the adoption of metal stripe, the mesh refinement is set as “conformal variant 1” to get better convergence. A mode source is applied to launch specified mode in the z direction. The “Pabs_adv” analysis group is utilized to calculate the absorption rate in the Au stripes. By utilizing the “mode expansion” monitor at the output port, we can obtain the normalized power of the specified mode (i.e., transmittance for specified mode) we are concerned about. In addition, precise meshes are essential in the Au stripe regions (and around) for the reason that the optical field near the metal region is strong and dissipates quickly in the direction away from the metal/dielectric interface. We set individual meshes with dimensions slightly larger than the Au stripes, as shown in Fig. 7(b). In addition, we test the simulation accuracy with different grid settings (override x/y mesh- dx/dy). As shown in Fig. 7(c)(d), a low-precision mesh may provide an underestimated absorptance, since the sum of absorptance and transmittances across all planes is far below 100%. In addition, there are more stringent requirements on the mesh accuracy for longitudinal direction (y -direction) in our simulation. In general, a mesh of 2 nm/1 nm is sufficient to

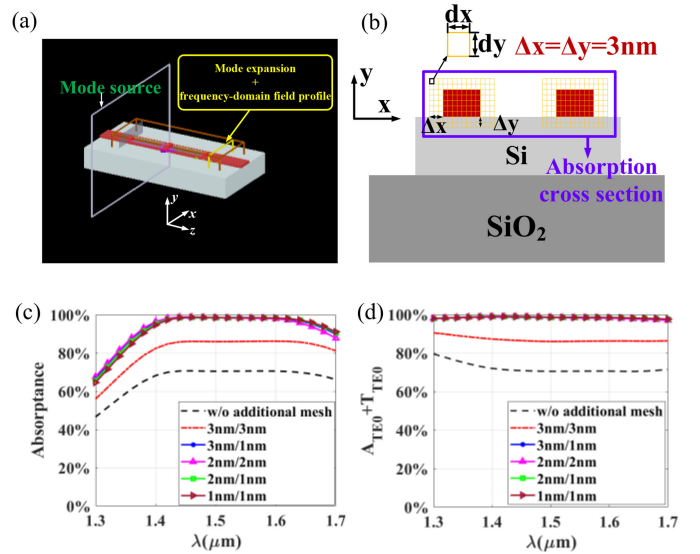


Fig. 7. (a) Perspective view of the numerical simulation software; (b) cross-section of absorption region and precise mesh settings around Au stripe; (c) absorption rate (A_{TE_0}) and (d) sum of absorbance (A_{TE_0}) and transmittance of TE₀ mode (T_{TE_0}) under TE₀ incidence for dual-metal stripe TE₂ mode pass filter with meshes (dx/dy) of different precision.

achieve high precision while ensuring an acceptable computational time. By utilizing a computer with Intel Core i7-6700K and a 32G RAM, 12~14 hours are required for the simulation of the TE₂ mode pass filter under certain incident conditions.

C. Fabrication Error Analyses

Despite the simulation results manifest remarkable performances of our proposed structures, it is still necessary to evaluate the fluctuations of key criteria caused by actual manufacturing inaccuracies, such as the metal width errors induced by pattern transfer/etching processes and film thickness deviations originated from non-ideal metal deposition. Here we consider the condition when Au stripe width error (Δwt) of ± 10 nm and thickness error (Δhm) of ± 1 nm are respectively introduced in

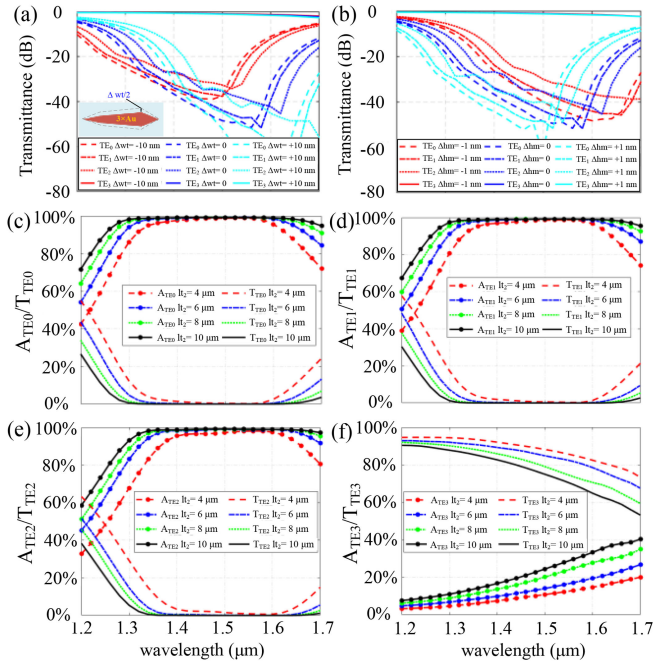


Fig. 8. Transmittance spectra (a) with Au stripes width error $\Delta wt = \pm 10$ nm; (b) with Au stripes thickness error $\Delta hm = \pm 1$ nm. Absorbance (A_{TEi}) and transmittance of specified mode (T_{TEi}) under different propagation decay lengths ($lt_2 = 4, 6, 8, 10 \mu\text{m}$) for various incidences: (c) TE_0 ; (d) TE_1 ; (e) TE_2 ; (f) TE_3 .

our proposed TE_3 mode pass filter ($w_{Si} = 1.6 \mu\text{m}$). As shown in Fig. 8(a), there would be a redshift of ~ 60 nm for the transmission spectrum with a 10 nm increase of wt . When the film thickness error is $-1 \text{ nm}/+1 \text{ nm}$, the transmission spectra would have a 60 nm red/blue shift, as shown in Fig. 8(b), which is consistent with the general law that a thinner metal film corresponds to a narrower ‘hybridization width’ for a fixed wavelength. One conclusion can be drawn is that a 1 nm thickness error usually can be roughly compensated by a 10 nm width offset for Au stripes. In addition, the propagation decay length indeed affects the performance of the mode filter. We tailor lt_2 and get device performances under TE_0 - TE_3 mode incidences. As shown in Fig. 8(c)-(f). A longer propagation decay length would result in larger absorption by Au stripes and wider operation wavelength span (see Fig. 8(c)-(e)), but it leads to a deterioration of EL for the desired HOM (Fig. 8(f)) simultaneously.

REFERENCES

- [1] P. J. Winzer, D. T. Neilson, and A. Chralyvy, “Fiber-optic transmission and networking: The previous 20 and the next 20 years,” *Opt. Exp.*, vol. 26, no. 18, pp. 24190–24239, 2018.
- [2] B. Stern *et al.*, “On-chip mode-division multiplexing switch,” *Optica*, vol. 2, no. 6, pp. 530–535, 2015.
- [3] L. W. Luo *et al.*, “WDM-compatible mode-division multiplexing on a silicon chip,” *Nat. Commun.*, vol. 5, no. 1, 2014, Art. no. 3069.
- [4] J. Wang, S. L. He, and D. X. Dai, “On-chip silicon 8-channel hybrid (de)multiplexer enabling simultaneous mode- and polarization-division-multiplexing,” *Laser Photon. Rev.*, vol. 8, no. 2, pp. L18–L22, 2014.
- [5] D. X. Dai *et al.*, “10-channel mode (de)multiplexer with dual polarizations,” *Laser Photon. Rev.*, vol. 12, no. 1, 2018, Art. no. 1700109.
- [6] X. R. Wu, C. R. Huang, K. Xu, C. Shu, and H. K. Tsang, “Mode-division multiplexing for silicon photonic network-on-chip,” *J. Lightw. Technol.*, vol. 35, no. 15, pp. 3223–3228, 2017.

- [7] N. Abadía *et al.*, “CMOS-compatible multi-band plasmonic TE-pass polarizer,” *Opt. Exp.*, vol. 26, no. 23, pp. 30292–30304, 2018.
- [8] K. T. Ahmed, H. P. Chan, and B. H. Li, “Scalable selective high order mode pass filter architecture with asymmetric directional couplers,” *Opt. Exp.*, vol. 28, no. 19, pp. 28465–28478, 2020.
- [9] K. T. Ahmed, H. P. Chan, and B. H. Li, “Broadband high-order mode pass filter based on mode conversion,” *Opt. Lett.*, vol. 42, no. 18, pp. 3686–3689, 2017.
- [10] C. L. Sun, W. H. Wu, Y. Yu, X. L. Zhang, and G. T. Reed, “Integrated tunable mode filter for a mode-division multiplexing system,” *Opt. Lett.*, vol. 43, no. 15, pp. 3658–3661, 2018.
- [11] Q. D. Huang, W. Wang, W. Jin, and K. S. Chiang, “Ultra-broadband mode filter based on phase-shifted long-period grating,” *IEEE Photon. Technol. Lett.*, vol. 31, no. 13, pp. 1052–1055, Jul. 2019.
- [12] M. Teng *et al.*, “Phase insensitive high order mode pass filter with low reflection for two-mode division multiplexing,” in *Proc. Opt. Fiber Commun. Conf.*, 2019, pp. 1–3.
- [13] X. W. Guan, Y. H. Ding, and L. H. Frandsen, “Ultra-compact broadband higher order-mode pass filter fabricated in a silicon waveguide for multi-mode photonics,” *Opt. Lett.*, vol. 40, no. 16, pp. 3893–3896, 2015.
- [14] Y. He, Y. Zhang, H. W. Wang, and Y. K. Su, “On-chip silicon mode blocking filter employing subwavelength-grating based contra-directional coupler,” *Opt. Exp.*, vol. 26, no. 25, pp. 33005–33012, 2018.
- [15] Y. Jung, S. U. Alam, and D. J. Richardson, “All-fiber spatial mode selective filter for compensating mode dependent loss in MDM transmission systems,” in *Proc. Opt. Fiber Commun. Conf.*, 2015, pp. 1–3.
- [16] Q. D. Huang and K. S. Chiang, “Polarization-insensitive ultra-broadband mode filter based on a 3D graphene structure buried in an optical waveguide,” *Optica*, vol. 7, no. 7, pp. 744–745, 2020.
- [17] Z. S. Chang and K. S. Chiang, “Ultra-broadband mode filters based on graphene-embedded waveguides,” *Opt. Lett.*, vol. 42, no. 19, pp. 3868–3671, 2017.
- [18] Z. K. Xing *et al.*, “Waveguide-integrated graphene spatial mode filters for on-chip mode-division multiplexing,” *Opt. Exp.*, vol. 27, no. 14, pp. 19188–19195, 2019.
- [19] P. Xing, K. J. A. Ooi, and D. T. H. Tan, “Ultra-broadband and compact graphene-on-silicon integrated waveguide mode filters,” *Sci. Rep.*, vol. 8, no. 1, pp. 9874–9879, 2018.
- [20] T. Y. Huang, Z. P. Pan, M. M. Zhang, and S. N. Fu, “Design of reconfigurable on-chip mode filters based on phase transition in vanadium dioxide,” *Appl. Phys. Exp.*, vol. 9, no. 11, 2016, Art. no. 112201.
- [21] G. Q. You and D. S. Gao, “Inverse designed ultra-compact broadband high-order mode filter,” *J. Phys. Conf. Ser.*, vol. 1213, no. 4, 2019, Art. no. 42059.
- [22] J. Q. You *et al.*, “Ultra-compact and low loss on chip higher order mode pass filter based on topology optimization,” *Appl. Phys. Exp.*, vol. 13, no. 2, 2020, Art. no. 22005.
- [23] Y. Tang, Z. Xi, M. Xu, S. M. B. Bäumer, A. J. L. Adam, and H. P. Urbach, “Spatial mode-selective waveguide with hyperbolic cladding,” *Opt. Lett.*, vol. 41, no. 18, pp. 4285–4288, 2016.
- [24] W. F. Jiang, J. Y. Miao, T. Li, and L. H. Ma, “Low-loss and broadband silicon mode filter using cascaded plasmonic BSWGs for on-chip mode division multiplexing,” *Opt. Exp.*, vol. 27, no. 21, pp. 30429–30440, 2019.
- [25] Lumerical. [Online]. Available: <https://www.lumerical.com/cn/>
- [26] E. D. Palik, *Handbook of Optical Constants of Solids*, Amsterdam, The Netherlands: Elsevier, 1985.
- [27] A. Akbari, A. Olivieri, and P. Berini, “Subbandgap asymmetric surface plasmon waveguide schottky detectors on silicon,” *IEEE J. Sel. Top. Quantum Electron.*, vol. 19, no. 3, May/Jun. 2013, Art. no. 4600209.
- [28] D. X. Dai and M. Zhang, “Mode hybridization and conversion in Silicon-Insulator nanowires with angled sidewalls,” *Opt. Exp.*, vol. 23, no. 25, pp. 32452–32464, 2015.
- [29] D. X. Dai, Y. B. Tang, and J. E. Bowers, “Mode conversion in tapered submicron silicon ridge optical waveguides,” *Opt. Exp.*, vol. 20, no. 12, pp. 13425–13439, 2012.
- [30] J. S. Guo, Z. W. Wu, and Y. L. Zhao, “Enhanced light absorption in waveguide schottky photodetector integrated with ultrathin metal/silicic stripe,” *Opt. Exp.*, vol. 25, no. 9, pp. 10057–10069, 2017.
- [31] Q. Li, J. J. Tu, Y. Tian, and Y. L. Zhao, “Polarization-insensitive waveguide schottky photodetectors based on mode hybridization effects in asymmetric plasmonic waveguides,” *Sensors*, vol. 20, no. 23, 2020, Art. no. 6885.
- [32] J. Sukham, O. Takayama, A. Lavrinenko, and R. Malureanu, “High-quality ultrathin gold layers with an APTMS adhesion for optimal performance of surface plasmon polariton-based devices,” *ACS Appl. Mater. Interfaces*, vol. 9, no. 29, pp. 25049–25056, 2017.
- [33] D. I. Yakubovskiy *et al.*, “Ultrathin and ultrasoft gold films on monolayer MOS_2 ,” *Adv. Mater. Interfaces*, vol. 6, no. 13, 2019, Art. no. 1900196.